Article:
Zhao, W, Wang, C, Zhang, T et al. (3 more authors) (2016) Effects of laser surface melting on erosion-corrosion of X65 steel in liquid-solid jet impingement conditions. Wear, 362-63. pp. 39-52. ISSN 0043-1648

https://doi.org/10.1016/j.wear.2016.05.006

Effects of laser surface melting on erosion-corrosion of X65 steel in liquid-solid jet impingement conditions

Weimin Zhao[1,2*], Chun Wang[2], Timing Zhang[1], Min Yang[1], Bin Han[1], Anne Neville[2]

1 College of Mechanical and Electronic Engineering, China University of Petroleum, Qingdao 266555, China

2 Institute of Functional Surfaces (iFS), School of Mechanical Engineering, University of Leeds, Leeds LS2 9JT, United Kingdom

Abstract: Laser Surface Melting (LSM) has the potential to increase the resistance of steels to erosion-corrosion. In this study a submerged jet impingement system containing a brine under saturated CO_2 conditions with sand has been used to assess the effect of LSM on the erosion-corrosion resistance of X65 steel. Erosion-corrosion rates under different experimental conditions were deduced based on CFD-simulated results and surface profile measurements. Scanning Electron Microscopy (SEM) was used to observe the morphology of erosion-corrosion damage. The results show that the erosion-corrosion rates at various impact angles can be decreased by LSM. Changes in microstructure, corrosion behaviour and hardness of X65 steel induced by laser treatment were analyzed by using optical microscopy, Transmission Electron Microscopy (TEM), Energy Dispersive X Ray analysis (EDX) together with electrochemical polarization and hardness distribution measurements, in order to clarify how laser treatment imparts the effects on the steel.

Keywords: steel; surface preparation; erosion-corrosion; impingement attack; multiphase.

* Corresponding author. Add: 66 Changjiang West Road, Qingdao 266580, Shandong province, China mainland; Tel.: +86-53286983503-8506.

E-mail address: zhaowm@upc.edu.cn

1. Introduction

Researchers describe pipeline networks as the arteries and veins of modern civilization [1]. For example, marine pipelines for the transportation of oil and gas are a safe and reliable part of the expanding infrastructure put in place for the development of the valuable resources below the world's seas and oceans [2]. The medium flowing from remote reservoirs to the extraction plant is a mixture of oil, gas, water and sand. The water usually contains very aggressive corrosive species (mainly Cl^-) and dissolved gases (such as CO_2, H_2S), and the aggressiveness of the environment is enhanced by the flowing conditions, particularly when sand is involved. This is because flow has the possible effect of breaching any protective or semi-protective corrosion product films and increasing the mass transfer rates close to the pipe wall [3] while sand particles can result in mechanical erosion attack on pipeline steel [4]. Erosion and corrosion are often synergistic, so the overall damage is normally higher than the summation of pure erosion and corrosion [4]. Problems due to erosion-corrosion are expected to increase in the future due to the increased water cut as wells age and the increase of sand production.

Various types of test rigs have been developed over the years to simulate erosion-corrosion failure processes in industry. Zeng [5] studied the erosion-corrosion behaviour of X65 carbon steel elbows by using electrode array techniques, the percentages of four components of damage (pure corrosion, pure erosion, erosion enhanced corrosion and corrosion enhanced erosion) were determined to reveal the dominant factors in erosion-corrosion at different locations in the elbow. By using a large scale (4-in.) flow loop to simulate real field conditions, Malka [6] investigated the interaction between corrosion and

erosion processes and quantified the synergism in realistic flow environments. The jet impingement apparatus [7-9] are also widely used by many researchers over a long period. According to the literature, the fundamentals of how erosion-corrosion system variables, such as temperature [10], impact angle [11], particle velocity [12], alloy composition [13] and chemicals [14], can affect erosion-corrosion rates are well discussed in terms of aqueous erosion-corrosion systems. The differences between total erosion-corrosion and the separate effects are analyzed [12]. However, the mechanism of erosion-corrosion has not been thoroughly understood because of the complexity of various erosion-corrosion systems. Moreover, the damage caused by the interaction of corrosion and erosion is still a serious concern.

To decrease the erosion-corrosion rate in a multiphase flow environment, the use of corrosion resistant alloys (CRAs) has been considered as an effective choice [4, 15, 16]. High capital expenditure costs are the factor limiting the use of CRAs. The use of carbon steel in conjunction with corrosion inhibitors in preventing erosion-corrosion has been observed as an economical viable solution for oil and gas pipelines. Many efforts have been made to develop effective inhibitors and determine their mechanism of action [17, 18]. However, corrosion inhibitors cannot efficiently mitigate the consequential damage of carbon steel under severe erosion-corrosion conditions, such as a high flow velocity, sand loading, more Cl^- etc. Improving surface properties of carbon steel by surface engineering technologies has become the focus of much research including carburizing [19], Ni-P and Ni-Cu-P electroless plating [16], Ni-based alloy electroplating [20, 21], and applying sprayed coatings [22-25]. Optimum application of surface engineering techniques can allow a remarkable improvement in the

surface hardness and the wear and corrosion resistance of carbon steel, without degradation of their bulk properties, and the cost can be much lower than using CRA bulk materials.

The Laser Surface Melting (LSM) process, as an advanced and economical manufacturing method, is a promising technology for improving the erosion-corrosion resistance of pipeline steel. As a heat source with high energy density, the laser is cheap and safe, since the laser beam can be transmitted through air rather than requiring a vacuum, and X-rays are not generated. Only the surface layer of steel is brought to a molten state by the laser in LSM, and the melted material then solidifies in a strongly non-equilibrium condition. LSM need not involve a change in the overall chemical compositions and so needs no additional expensive materials; thanks to the rapidity of the heating rate, it does not require a quenching medium, as the material surrounding the heated layer acts as a heat sink, which leads to “self-quenching” [26]. Tooling can be designed to guide the laser to the inner walls of pipe, and oil well tubing with small diameter has been successfully surface treated [27]. LSM can be extremely selective and almost without distortion; it produces fine metastable phase for the microstructure transformation occurring in non-equilibrium state, which achieves higher levels of hardness [28] and may change erosion, corrosion or other properties. Besides, LSM can be easily used to treat just the potential erosion-corrosion serious area of pipeline, such as bends or different regions in welded joints [29], in order to remove the susceptible parts of the pipeline and ensure the service life of every part tends to accordance. Using selective treatment can also reduce capital expenditure costs.

The purpose of this research was to evaluate the feasibility of applying LSM to improve the erosion-corrosion resistance of low carbon steel. In this paper, X65 pipeline steel was

treated by LSM, and erosion-corrosion experiments were carried out in a simulated multiphase flow environment in order to find out low performing locations and study the effects of LSM on the erosion-corrosion behaviour of X65 steel. Microstructure observation, hardness tests and electrochemical corrosion tests were carried out together with SEM observation of the erosion-corrosion surfaces, so that the mechanism by which LSM can affect the erosion-corrosion behaviour could be determined.

2. Material and experimental methods

2.1 Materials and test specimens

The steel used in the current study is pipeline steel API-5L-X65 which contains 0.12% C, 0.19% Si, 1.33% Mn, 0.007% P, 0.0020% S, 0.12% Cr, 0.18% Mo, 0.04% Ni, 0.05% Cu, 0.004% Sn, 0.028% Al, < 0.0005% B, 0.008% N, 0.035% Nb, 0.0005% Ti, 0.054% V, and the balance is Fe. This steel in supply state was hardened at 920 ºC for 2 hours (water quenched) and tempered at 550 ºC for 2 hours (air cooled).

The specimens used in the static corrosion and erosion-corrosion tests are flat disks, and the diameter is 25 mm while the thickness is 6 mm. About half of the specimens remain in the supply state, and others were surface melted using a commercial available continuous wave CO_2 laser. Laser parameters were optimized by preliminary tests. The final determined laser power was 1300 W, scanning speed was 2000 mm/min, the width of the laser band was 3 mm, and the overlapping ratio of laser band was 10%.

The test surfaces of all the specimens were subsequently ground with 1200-grit sand paper. Thereafter, the specimens were polished using 1 μm diamond paste and successively rinsed and cleaned with deionized water and acetone. The microstructure of as-supplied steel

and laser surface-treated steel were observed by LEICA DM2500M optical microscope and FEI Tecnai G2 F30 S-TWIN TEM. Phase distribution in laser-treated X65 steel was predicted by Finite Element Modeling (FEM) simulation. A transient 3D LSM calculation model based on a commercial finite element code SYSWELD, which considered a band distribution of heat flux using a moving heat source, was established to simulate the microstructure evolution. The methodology of FEM simulations was described in detail in study [26]. Hardness tests were carried out using HV1000-A hardness testing machine.

2.3 Erosion-corrosion experiments

Erosion-corrosion measurements were carried out in a circulating jet impingement system as shown in Fig.1 [29, 30]. A mixture of fluid saturated with CO_2 and sand particles is delivered through an upright dual nozzle system impinging on to a flat specimen surface. The nozzle diameter was 4 mm. The distance between the nozzle and the specimen was kept at 5 mm. The electrochemical setup combined with the jet impingement system enables the in situ Linear Polarization Resistance (LPR) to be measured.

The test fluid used in this study was synthetic Forties Brine (typical of the Forties Field in the North Sea) which was saturated with CO_2, and contained 15.69g/L $CaCl_2 \cdot 6H_2O$, 4.47g/L $MgCl_2 \cdot 6H_2O$, 0.875g/L KCl, 74.7g/L NaCl, 0.446g/L $BaCl_2 \cdot 2H_2O$, 1.44g/L $SrCl_2 \cdot 6H_2O$, 0.335g/L $NaHCO_3$. Before commencing the erosion-corrosion test, the fluid was purged with CO_2 for 12 h to remove the dissolved oxygen. Silica sand particles with average diameter of 250 μm were added into the fluid. After 4 hours tests, SEM image of the sand particles were compared with the sand particles prior to tests as shown in Fig. 2. It has been shown that there is no significant degradation of the sand in 4 hours circulation of the

impingement tests. The vessel was then sealed and the erosion-corrosion test was started, CO_2 was continuously bubbled with three bubbles per second throughout the duration of the tests. The jet impingement velocity was 20 m/s, the temperature of the test fluid was set at 50 ºC and controlled by an automatic temperature control system. The sand concentration coming out from the nozzles was 1000 ppm. From previous study, in the position with highest erosion-corrosion rate on the sample, the wall shear stress is 508 Pa at 50°C and the Reynolds number is 14465 [17].

Erosion-corrosion tests were conducted for 4 h and repeated three times using altogether six specimens, in which three specimens were used to determine weight loss rate and the other three were used for Linear Polarization Resistance (LPR) measurements. The corrosion products were removed from the test surface with Clarkes' solution [18] after erosion-corrosion tests. Three specimens were weighted before and after the experiments to determine the total weight loss of each specimen, then the average erosion-corrosion rate was calculated based on the surface area of 4.9 cm^2 (corrosion happened across the whole exposed metal surface). To further determine the erosion-corrosion rates at different experimental conditions, local particle impact velocity and impact angle at the surface of the specimen were predicted by Computational Fluid Dynamics (CFD) simulations together with surface profile measurement. The methodology of CFD simulations was described in detail in a previous study [32]. Top view of the test sample after testing viewed under the naked eye indicating three distinctive regions of wear and also the CFD predictions of particle motion in the impingement system are shown in Fig.3. There is a distance 5 mm between the nozzle and the specimen, and fluid outflow from the nozzle to specimen surface has a divergence angle.

Erosion-corrosion, especially corrosion, happened across the whole exposed metal surface. Specimens after erosion-corrosion tests were examined by a Carl Zeiss EVD MA15 scanning electron microscope (SEM) and a JXA-8230 electron probe micro-analyser (EPMA).

In order to study the effect of erosion on corrosion behaviour, the corrosion rates coming from LPR measurements in erosion-corrosion are compared with those from electrochemical experiments under static corrosion. The static corrosion tests were performed by using M398 Electrochemical Testing System in a conventional three-electrode cell system. A saturated calomel electrode (SCE) was used as reference electrode and a platinum sheet as counter electrode. The X65 steel specimen was used as working electrode. The test fluid was synthetic Forties Brine. All the tests were conducted at 50±1 ℃. The specimens were immersed in the corrosive environment at open circuit potential (OCP) for one hours prior to Tafel polarization measurement. Polarization curve was acquired by scanning the potential range from -250 mV (vs. OCP) to 250 mV at a scanning rate of 0.166 mV s^{-1}. The corrosion current density (i_{corr}) was calculated using PARCalc Tafel analysis routine based on the nonlinear least-square method. Three repeated polarizations were conducted.

3 Results

3.1 Erosion-corrosion behaviour

3.1.1 Erosion-corrosion rates

The average of total erosion-corrosion rates derived from the weight-loss rate, for the X65 steel with and without LSM in CO_2 saturated Forties Brine at 20 m/s, 1000 ppm sand loading, are shown in Table 1. The standard errors with 95% confidence interval were calculated on the basis of three repeated measurements. The erosion-corrosion rate of the steel

can be effectively reduced by LSM, and it can be deduced that the erosion-corrosion rate is decreased by 44.2%.

Table 1 Erosion-corrosion rate for the steel before and after LSM

Material	Erosion-corrosion rate, mmpy
As-supplied steel	23.68±1.43
Laser surface treated steel	13.22±3.12

Specimens after erosion-corrosion tests were examined by a Bruker optical profile system NPFLEX. The erosion-corrosion indentation was round at the surface (Fig.4(a)), and Fig.4(b) shows one profile measurement result along a line which runs across the erosion-corrosion indentation center of as-supplied X65, and one measurement result for a laser surface treated specimen. It is obvious that the depth of erosion-corrosion indentation varies with position along the surface.

Since the erosion-corrosion indentation showed relatively good symmetry (Fig.4), we shall assume the indentations are symmetric. The centre of the erosion-corrosion indentation was found, and then the average of readings which were equidistant from the centre was calculated. The local erosion-corrosion rates at different positions could be calculated by dividing the indentation depth by total test time (4h) (see Fig.5). The erosion-corrosion rates show first rising then falling to a stable value from centre to outside of indentation on specimen, and erosion-corrosion focus on the centre area about 3 mm in radius. Therefore, the average erosion-corrosion rates across the whole exposed surface listed in Table 1 are much lower than those data around indentation shown in Fig. 5. It can be seen from Fig. 5 that the local erosion-corrosion rates of the laser surface treated specimens were lower than those of

the as-supplied specimens, and this demonstrated once again LSM could improve the resistance to erosion-corrosion of X65.

Fig.6 present local particle impact data at the surface of the specimen as predicted by CFD simulations for Forties Brine at 20m/s. Based on the data corresponding to the curves in Fig.5, combined with the local sand particle impact data showed in Fig.6, the local erosion-corrosion rates at different impact angles could be deduced. First, the equations from fitting curves in Fig.6 were determined.

$$y=-0.2931x^3+5.1999x^2-33.297x+91.184 \qquad R^2=0.9991 \qquad (1)$$

in which y is impact angle (degree) and x is distance from the center of indentation (mm). Since the erosion-corrosion rates at various values of x are known (Fig.5), combined with equation (1), it was easy to obtain the erosion-corrosion rates at various impact angles (Fig.7).

The information given in Fig.7 is useful for designers to find the susceptible parts of the pipeline and LSM could be applied in order to improve local erosion-corrosion resistance. It can be seen from Fig.7 that the erosion-corrosion rate for as-supplied X65 remains small if the particle impact angle is less than 26°, and increases greatly between 26° and 44°, then remains very high value and drops slightly when the impact angle is between 44° and 90°, the highest erosion-corrosion rate is achieved at 44°. The laser surface-treated specimen showed a similar trend to the as-supplied specimen with a slight change of impact angles, with the highest erosion-corrosion rate achieved at 42°. LSM can significantly reduce the erosion-corrosion rate in the range of 26° to 90°. Therefore, LSM can be applied in the bends of as-supplied pipeline where the flow direction changes by more than 26°.

3.1.2 Surface examination by SEM

Since the erosion-corrosion indentation was relatively symmetric (see Fig.4), a line across the indentation center of the specimen was drawn using a marker pen, and a Carl Zeiss EVD MA15 SEM was used to observe the surface morphology along the line. Possible changes in morphology caused by different impact angles and the effects of LSM could be determined. There were three main regions on the test surface (see Fig.5): (1) Region 1, Impact angle 90° to 42° (high to medium range), with high erosion-corrosion rate; (2) Region 2, Impact angle 42° to 26° (medium to low range), with dramatically changing erosion-corrosion rate; (3) Region 3, Impact angle < 26° (low to sliding range), with very low erosion-corrosion rate. Assuming α represents impact angle, typical pictures in these three regions are shown in Fig.8 to Fig.10.

Fig.8 shows the erosion-corrosion morphology in the region 1. In the centre of indentation where sand in CO_2 saturated Forties Brine impact the surface at a normal angle, there were no furrows caused by ploughing and cutting on the surfaces of X65 with and without laser treatment (Fig.8(a)(b)). With a decrease in impact angle, the horizontal velocity component increases which causes cutting wear, but there were still no cutting wear furrows (Fig.8(c)(d)) until the impact angle reached 42° to 45° corresponding to the highest erosion-corrosion rate (Fig.7). In the zone where impact angles were lower than 45°, there were some cutting wear furrows, but these wear furrows were very slight (Fig.8(e)(f)). Obviously corrosion happened on the surface of as-supplied X65 (corrosion products show as non-conductive white substances), and the corrosion became more severe with the decrease in impact angles (Fig.8(a)(c)(e)).

When the impact angle decreases to lower than 42°, scars of ploughing and cutting

become clear and gradually severe with the decrease in impact angles (Fig.9), and corrosion of as-supplied X65 looks slight compared to that at high impact angles (Fig.8 and Fig.9). It seems that erosion plays a more important role in erosion-corrosion failure in this zone. The scratches on laser-treated specimens are narrower than that on X65 in as-supplied state, therefore, the resistance to erosion is better for laser-treated X65.

When the impact angle decreases to lower than 26°, the normal velocity component is very small and sand impacting effects can be neglected. Fig.10 shows the typical erosion-corrosion morphology in this region. The multiphase medium slides along the metal surface and cause cutting wear. No obvious corrosion can be observed.

3.1.3 Cross-sectional examination

A X65 steel specimen was cut by wire electrical discharge machining (WEDM) with the cross-section through the erosion-corrosion indentation. After grinding, polishing and etching, the cross section was examined by a JXA-8230 electron probe micro-analyser (EPMA) with step size of 0.5 mm. The observation positions are shown in Fig. 11(a), and the microstructures in corresponding positions are shown in Fig. 11(b) to Fig. 11(h).

Plastic flow induced by erosion could be observed from subsurface morphology. It seems that there is a plastic deformation layer about 5 μm thick in the centre of erosion-corrosion indentation (Fig.11(b)). Numerous sand particles impact the surface at a normal angle repeatedly during 4 h impingement, and the cumulative effects result a plastic layer that has a distinctive boundary from normal microstructure. Plastic flow lines appear with decreased impact angle, see from Fig.11(c) to Fig.11(h). The thickness of plastic layer gradually increase from position c to position e, and the density of plastic flow lines decreases with increased

distance from surface, see Fig.11(c) to Fig.11(e). The amount of plastic deformation decrease when impact angle is lower than 45°, see Fig.11(f) to Fig.11(h). Cracks and pit can be found in plastic layer (Fig.11 (c) and Fig.11 (g)).

3.2 Microstructure observation and hardness measurement

Erosion resistance of one material is directly related to its hardness, while hardness is dependent on microstructure.

3.2.1 Microstructure

The microstructure of as-supplied X65 steel is composed of equiaxed ferrite and small amount of irregular polygonal ferrite, and many small precipitates dispersed in the matrix, see Fig.12(a). Fig.12(b) shows its fine structure obtained from TEM observation, and the substructure of ferrite is tiny equiaxed ferrite. EDX was used to analyze the element composition of phase A in Fig.12(b), and the results show that the precipitates are mainly composed of carbide containing Nb, Ti, V (Fig.13).

Because of the low carbon content, no cracks appeared in laser-treated X65 steel (Fig.14). Laser-treated layer includes melted zone and heat-affected zone (HAZ) (Fig.14(a)). The thickness of melted zone is about 150 μm (Fig.14(b)), among which the adjacent to HAZ is planar crystal area, the more distant surface area is dentrite crystal zone. In HAZ, the zones outward from fusion line are, in order, coarse grain zone (Fg.12(c)), fine grain zone (Fig.14(d)) and partially refined grain zone (Fig.14(e)). Coarse grain zone usually has the lowest properties because of its coarse grains, however, the problem is not especially serious in laser-treated steel. Due to the laser heating being a process of rapid heating, the original Nb, Ti or V carbides in steel have no time to decompose, and these carbides can effectively

prevent the growth of austenite grains in the overheated zone. The addition of Cr and Mo in pipeline steel can improve the toughness and strength of HAZ [33]. Within the scope of the HAZ, the density of strengthening phase is higher than that in base material. The Nb, Ti or V carbides can effectively improve the strength of steel.

SYSWELD software was used to simulate the LSM process on X65 steel, and the microstructure evolution was predicted. Fig.15 shows the final phase distribution in the laser-treated steel along the thickness direction, and only ferrite and martensite present there. It is obvious that the microstructure in the as-supplied steel is composed of ferrite, which is consistent with the observed results shown in Fig.16. The ferrite is completely transformed to martensite in the melted zone. The proportion of martensite in HAZ gradually decreases with the increase in distance from melted zone. The overall thickness of melted zone and HAZ is near 800 μm at the center of laser band, this data is consistent with the observed results shown in Fig.14(a). In order to verify the accuracy of the calculation results, the melted zone was examined by TEM, see Fig.16(a). The microstructure in the melted zone shows like lath. There are film-like black phases between laths, and the black phase within B area in Fig.16(a) was characterized as retained austenite by selected area diffraction (Fig.16(b)). This morphology, thin layers of retained austenite present between the laths, means the typical microstructure in melted zone is lath martensite [34]. There are many dislocations in lath martenite, and the density of dislocations is not uniform; dislocations pile up locally. Because of dislocation strengthening and solution strengthening, lath martensite has high strength, hardness and certain toughness, plasticity [35].

Properties of steel are determined by its microstructure. Since LSM treatment can change

the grain size, the quantity and distribution of strengthening phases, the presence of lath martensite in X65 steel, therefore, the hardness, corrosion and erosion-corrosion behaviour would change after LSM treatment.

3.2.2 Hardness

The LSM treated specimen was cut by wire electrical discharge machining (WEDM) with the cross-section perpendicular to the direction of laser band, see Fig.17(a). After grinding and polishing, the hardness distribution of cross section was tested using microhardness tester. The range of tested width is from the longitudinal centre line of one laser band to the next longitudinal center line, and range of tested depth is from the melted surface down to original base metal. Fig.17(b) shows the obtained cross-section hardness distribution. The tested data show that the hardness of as-supplied X65 steel is from 172 $HV_{0.3}$ to 180 $HV_{0.3}$, and that of melted zone is from 470 $HV_{0.3}$ to 538 $HV_{0.3}$. The hardness in the HAZ gradually decreases from the melted zone, through HAZ, down to base metal. The thickness of the layer, whose hardness is higher than that of base metal, is between 450 μm and 800 μm. The maximum and minimum thickness of the layer, with high hardness, appears in the centre of laser band and overlapping zone, respectively.

From the microstructure analysis results, the microstructure in the melted zone is found to consist of lath martensite, and this zone has the highest hardness although the amount of strengthening phase is small. The proportion of martensite in the HAZ gradually decreases with the increase in distance from the fusion line, and the corresponding hardness gradually decreases. It can be deduced that the formation of lath martensite is the main factor that influences the hardness, and the hardness is determined by its proportion.

There is a linear correlation between the accelerated erosion and surface hardness degradation for carbon steel [36], since LSM can greatly improve the surface hardness of X65 steel, therefore, erosion resistance significantly enhanced after LSM treatment.

3.3 Corrosion behaviour

Corrosion in erosion-corrosion is induced by two reasons. First is the pure electrochemical process, and the second is enhancement of corrosion due to erosion. Electrochemical corrosion behaviour was carried out under static corrosion and erosion-corrosion states.

Tafel polarization tests of X65 steel before and after LSM treatment were carried out in static Forties Brine，and same tests were repeated three times. Typical polarization curves were shown in Fig.18. Laser treatment has no obvious influence on electrochemical corrosion behaviour, and both anodes are in active dissolution state. Corrosion current density was obtained by linear extrapolation, then using the following formula to calculate corrosion rate [37]:

$$V_d = \frac{3.27\times10^{-3}\, A i_{corr}}{n\rho} \quad (2)$$

Where V_d is the corrosion rate in loss of depth (mmpy). A is the atomic weight of the metal ($g\cdot mol^{-1}$). i_{corr} is corrosion current density ($\mu A\cdot cm^{-2}$). n is valence of the metal cation. ρ is density of the corroded material ($g\cdot cm^{-3}$). Based on the data of A, n and ρ for steel, the expression in formula (2) can be simplified to obtain the following expression:

$$V_d = 0.0117 i_{corr} \quad (3)$$

The calculated results of corrosion rates in static state, with standard error (95% confidence interval), are shown in Table 2.

Linear polarization resistance measurements were carried out in erosion-corrosion conditions to study the in situ corrosion processes of the materials, and the calculated results of corrosion rates are plotted as a function of time (see Fig.19). Average all the corrosion rates at different times to obtain the mean value for one experiment, then the corrosion rates in erosion-corrosion with standard error are shown in Table 2.

Table 2 Corrosion rates of X65 steel in static Forties Brine

Material	Corrosion rate, mmpy	
	In static state	In erosion-corrosion
As-supplied steel	0.37±0.04	9.34±0.73
laser treated steel	0.32±0.08	6.36±1.29

It can be seen from Table 2 that the corrosion rates of X65 steel under erosion-corrosion are much higher than those under static corrosion. Erosion caused by sand particles in a flowing solution obviously accelerates corrosion. Studies show that impingement process can introduce residual compressive stress and yield severe plastic deformation [38] that increase the surface roughness and defects density [39]. Consequently, the corrosion rate and the susceptibility to pit corrosion increased as roughness increased [40]. Besides, erosion can also remove the protective corrosion product film. Therefore, in multi-phase jet impingement conditions, corrosion rate of X65 steel significantly improved.

Table 2 also shows LSM treatment can improve corrosion resistance of X65 steel in erosion-corrosion. Corrosion rates change little in static Forties Brine, while corrosion rate decrease by 31.9% in erosion-corrosion process. The reason why LSM treatment can enhance corrosion resistance in erosion-corrosion is related to the improvement of hardness. It is well

known that the ability of plastic deformation is inversely proportional to the hardness of metal, and the harder material the less prone to plastic deformation. LSM treatment can significantly improve the hardness of X65 steel, therefore, the amount of erosion-induced plastic deformation is small. Since improvement of surface roughness and plastic strain decrease corrosion resistance [39], the corrosion rates of laser-treated X65 steel with high hardness is small in erosion-corrosion process. In other words, erosion induces improvement of surface energy and surface plastic deformation, which enhance corrosion, and the hardness improvement by laser treatment inhibits surface plastic deformation then decrease corrosion.

4. Discussion

Erosion-corrosion is a failure mode under the synergistic effects of corrosion and erosion. The total weight loss comes from four ways: corrosion (pure electrochemical process), erosion (pure mechanical damage, including critical strain, plastic deformation and material removal), the enhancement of corrosion due to erosion (impingement forces activate the material), the enhancement of erosion due to corrosion (corrosion decreases surface integrity and makes erosion easier). LSM can influence the erosion and erosion-enhanced corrosion behaviour of X65, and the relative contributions of corrosion and erosion in erosion-corrosion changes with impact angles. The acting mechanism of LSM will be discussed in the following paragraphs.

When the water jet impinges on the specimen, the oncoming fluid jet decelerates rapidly due to an orthogonal obstruction presented by the test surface leading to a significant drop in flow momentum in the direction normal to the surface. The jet impingement velocity was 20 m/s, but this velocity approaches to 0 m/s at the surface of test specimen when the impact

angle was 90° [41]. The kinetic energy of particles will convert into deformation energy and/or heat energy, and plastic deformation may occur on the impacting specimen (Fig. 11(b)). If the specimen is brittle material, the resulted plastic deformation surpasses the plastic deformation capacity, cracking appears on the specimen and the erosion rate will be high. However, the microstructure of X65 steel is ferrite (Fig.12) and that of surface melted layer is lath martensite (Fig.16), both have good plasticity and toughness. Work hardening can cause dislocation multiplication thus increase mechanical strength and decrease plasticity, and some cracks may occur in plastic layer. However, work hardening cannot change pipeline steel from plastic material to brittle material, therefore the erosion induced by brittle cracking is low. There is also no horizontal velocity component under impact angle of 90°, and the erosion induced by cutting wear action can be neglected. Erosion is not the controlling factor in erosion-corrosion in the centre of indentation. The main failure cause should be corrosion and erosion-enhanced corrosion. The corrosion rates of as-supplied and laser-treated X65 steel are similar under static state (see Table 2), so the difference in erosion-enhanced corrosion is the main reason why laser surface treatment can improve the erosion-corrosion resistance under impact angle of 90°. Erosion could induce the increase in surface roughness, plastic strain and defect density that result in a decrease in corrosion resistance [39]. There is no cutting wear action to remove corrosion products under vertical impinging condition, so the amount of retained corrosion products (non-conductive white substances under SEM observation) goes some way to reflect corrosion level. Only very little corrosion products appear on the surface of the laser-treated sample (Fig.8(b)), which means there is no serious corrosion. However, corrosion on the surface of as-supplied X65 is severe (see white bright corrosion products in

Fig.8(a)), which may be related to its low hardness. Low hardness is related to significant increase in plastic strain under direct impinging. Hardness testing shows that laser surface treatment could significantly improve the hardness of as-supplied X65 steel (see Fig.17), which improve erosion-enhanced corrosion resistance.

In the region with impact angles lower than 90°, the multiphase flow velocity of 20 m/s can be classified into a normal velocity component and a horizontal velocity component. The normal velocity component is high when the impact angle is higher than 45°, and there is still a significant drop in flow momentum in the direction normal to the surface [41]. Most of the kinetic energy of particles converts into deformation energy, which cause plastic deformation (see Figs. (c), (d) and (e)) or dislocation multiplication thus reduces the corrosion resistance. Severe corrosion happens on the deformed surface, however, the resulting corrosion products cannot stay in position which is different to that with an impact angle of 90°, because cutting wear action could remove corrosion products and/or surface materials leaving fresh surface there. Cutting wear is associated to the horizontal velocity component. Without the protection of corrosion products, the fresh surface will undergo direct impact and produce much more plastic deformation than the center of indentation, and much severe corrosion happens in this region (Fig.8). In region 1, severe corrosion of the deformed surface layer which is a result of impact in the normal direction plays more important role in erosion-corrosion failure. Cutting wear coming from the horizontal velocity direction facilitates corrosion, therefore there are only corrosion products and no obvious cutting wear furrows on the erosion-corrosion surface in region 1. From impact angle 90° to 42°, plastic deformation (density of flow lines) gradually decreases with the decrease in loss of flow momentum in the direction normal to the

surface, and this may induce the increase in corrosion resistance, however, the cutting action will strengthen gradually, and this may quicken the process of removing corrosion products and cause much more material loss. Therefore, the erosion-corrosion remains high and increases gradually (see Fig.7).

When the impact angle is less than 45°, the horizontal velocity component is larger than the normal velocity component, and most of the kinetic energy of particles tends to remove plastic steel material by ploughing and cutting action, rather than cause compressive plastic deformation and so enhance corrosion. Fig.20 demonstrates loss of material due to ploughing and cutting action occurring at low angle impacts [41]. For ploughing and cutting, the larger the arrival angle is, the larger the exit angle is. Therefore, those first wear scars (under impact angle from 45° to 30°) are small round with a dish-shaped cross section morphology. It can be seen clearly from the middle zone in Fig.9(b) the wear scar caused by material removal, and the shape of these scars are similar to the scars showed in Fig.20. The exit angle decreases gradually with the decrease in the arrival angle, and therefore the wear scar becomes long and flat (from Fig.9(a)(b) to Fig.8(c)(d)). It is obvious that ploughing and cutting wear will gradually play a more important role in erosion-corrosion failure in region 2.

When the impact angle is very low (<26°), the ploughing action can be neglected, and only cutting action removes the surface material. This loss rate depends on the wear resistance of the material. Generally speaking, laser surface hardening can improve wear resistance of hypo-eutectoid steels [42, 43].

LSM can significantly improve the hardness of X65 steel; therefore, it not only reduces the deformation and the resulted corrosion of deformed surface layer which is resulting from

impact in normal direction, but also reduces the ploughing and cutting wear. That is why LSM can reduce the erosion-corrosion rate under different impact angles from 90° to sliding range.

5. Conclusions

(1) LSM can change the microstructure of X65 steel from ferrite matrix to lath martensite, significantly improve hardness from about 175 $HV_{0.3}$ to around 500 $HV_{0.3}$, and obviously decrease corrosion rate and erosion-corrosion rate in multi-phase jet impingement conditions. The total erosion-corrosion rate of X65 steel can be decreased by 44.2%.

(2) When the impact angle is between 45° and 90° the erosion-corrosion rates remains high and gradually increases with decreasing impact angle and reaches the highest value at 42° to 45° from where erosion-corrosion rates decrease abruptly until a stable and low value around 26° is reached. LSM can reduce all the local erosion-corrosion rates of X65 steel under different impact angles.

(3) Plastic deformation and erosion-enhanced corrosion which results from impact in the normal direction together with ploughing and cutting wear associated with low angle impact play important role in the erosion-corrosion failure process. LSM can significantly improve the hardness of X65 steel, thus reduce plastic deformation and deformation-induced corrosion and resistance to ploughing and cutting wear. That is why LSM can improve erosion-corrosion behaviour of X65 steel.

Acknowledgements

Part of this work was financially supported by the China National Natural Science Funds (No. 51179202). The authors are grateful for the technical support on the impingement rig from the technicians at the University of Leeds.

References

[1] M. Shehadeh, M. Anany, K.M. Saqr, I. Hassan, Experimental investigation of erosion-corrosion phenomena in a steel fitting due to plain and slurry seawater flow, International Journal of Mechanical and Materials Engineering, 9 (2014) 22-29.

[2] Y. Bai, Q. Bai, Subsea pipelines and risers, Elsevier, 2005.

[3] A. Mohammed Nor, M.F. Suhor, M.F. Mohamed, M. Singer, S. Nesic, Corrosion of carbon steel in high CO2 containing environments - The effect of high flow rate, Corrosion 2012, March 11, 2012 - March 15, 2012, National Assoc. of Corrosion Engineers International, Salt Lake City, UT, United states, 2012, pp. 5340-5351.

[4] K. Alzawai, Understanding the role of erosion/corrosion interactions in degradation of steel and stainless steel alloys in systems containing sand and oil, The university of Leeds, Leeds, UK, 2011.

[5] L. Zeng, G.A. Zhang, X.P. Guo, Erosion–corrosion at different locations of X65 carbon steel elbow, Corrosion Science, 85 (2014) 318-330.

[6] R. Malka, S. Nesic, D.A. Gulino, Erosion-corrosion and synergistic effects in disturbed liquid-particle flow, Wear, 262 (2007) 791-799.

[7] P. Andrews, T.F. Illson, S.J. Matthews, Erosion-corrosion studies on 13Cr steel in gas well environments by liquid jet impingement, Wear, 233-235 (1999) 568-574.

[8] X.M. Hu, A. Neville, CO_2 erosion-corrosion of pipeline steel (API X65) in oil and gas conditions-A systematic approach, Wear, 267 (2009) 2027-2032.

[9] M. Abedini, H.M. Ghasemi, Synergistic erosion-corrosion behavior of Al-brass alloy at various impingement angles, Wear, 319 (2014) 49-55.

[10] M.M. Stack, S.M. Abdelrahman, B.D. Jana, Some perspectives on modelling the effect of temperature on the erosion-corrosion of Fe in aqueous conditions, Tribology International, 43 (2010) 2279-2297.

[11] N. Andrews, L. Giourntas, A.M. Galloway, A. Pearson, Effect of impact angle on the slurry erosion-corrosion of Stellite6 and SS316, Wear, 320 (2014) 143-151.

[12] M.A. Islam, Z.N. Farhat, The synergistic effect between erosion and corrosion of API pipeline in CO2 and saline medium, Tribology International, 68 (2013) 26-34.

[13] S.H.M. Anijdan, A. Bahrami, N. Varahram, P. Davami, Effects of tungsten on erosion-corrosion behavior of high chromium white cast iron, Mat Sci Eng a-Struct, 454 (2007) 623-628.

[14] A. Neville, C. Wang, Erosion–corrosion of engineering steels—Can it be managed by use of chemicals?, Wear, 267 (2009) 2018-2026.

[15] S. Aribo, R. Barker, X. Hu, A. Neville, Erosion–corrosion behaviour of lean duplex stainless steels in 3.5% NaCl solution, Wear, 302 (2013) 1602-1608.

[16] X. Fang, Y. Bai, Z. Wan, Erosion corrosion behaviour of J4 stainless steel and electroless plating coatings of Ni–P and Ni–Cu–P in liquid–solid two–phase flow, Acta Metall Sinica, 46 (2010) 239.

[17] C. Wang, Erosion-corrosion mitigation using chemicals, The University of Leeds, Leeds, UK, 2007.

[18] R. Barker, X. Hu, A. Neville, S. Cushnaghan, Inhibition of Flow-Induced Corrosion and Erosion-Corrosion for Carbon Steel Pipe Work from an Offshore Oil and Gas Facility, Corrosion, 69 (2013) 193-203.

[19] B. Saleh, S. Ahmed, Slurry Erosion–Corrosion of Carburized AISI 5117 Steel, Tribology Letters, (2013) 1-8.

[20] L.F. Jiang, S.Z. Yang, X.L. Ji, Y. Tang, P. Yuan, Y.L. Zhou, Erosion-corrosion of electroplated Ni-based alloy coatings, Zhendong yu Chongji(Journal of Vibration and Shock), 31 (2012) 137-142.

[21] X. Ji, J. Zhao, S. Yang, L. Gu, Erosion-Corrosion Behavior of Electrodeposited Amorphous Ni-WP Coating in Saline-Sand Slurry, Corrosion, 69 (2013) 593-600.

[22] Z. Zheng, Y. Zheng, W. Sun, J. Wang, Erosion–corrosion of HVOF-sprayed Fe-based amorphous metallic

coating under impingement by a sand-containing NaCl solution, Corrosion Science, 76 (2013) 337-347.
[23] G. Saha, T. Khan, G. Zhang, Erosion–corrosion resistance of microcrystalline and near-nanocrystalline WC–17Co high velocity oxy-fuel thermal spray coatings, Corrosion Science, 53 (2011) 2106-2114.
[24] W.M. Zhao, Y. Wang, C. Liu, L.X. Dong, H.H. Yu, H. Ai, Erosion–corrosion of thermally sprayed coatings in simulated splash zone, Surface and Coatings Technology, 205 (2010) 2267-2272.
[25] Y. Wang, Y. Zheng, W. Ke, W. Sun, W. Hou, X. Chang, J. Wang, Slurry erosion–corrosion behaviour of high-velocity oxy-fuel (HVOF) sprayed Fe-based amorphous metallic coatings for marine pump in sand-containing NaCl solutions, Corrosion Science, 53 (2011) 3177-3185.
[26] C. Li, Y. Wang, B. Han, Microstructure, hardness and stress in melted zone of 42CrMo steel by wide-band laser surface melting, Optics and Lasers in Engineering, 49 (2011) 530-535.
[27] G. Shi, Research and application on laser surface modification of sucker rod and tubing, China University of Petroleum, Qingdao, China, 2013.
[28] I. Iordanova, V. Antonov, S. Gurkovsky, Changes of microstructure and mechanical properties of cold-rolled low carbon steel due to its surface treatment by Nd : glass pulsed laser, Surf Coat Tech, 153 (2002) 267-275.
[29] X. Hu, R. Barker, A. Neville, A. Gnanavelu, Case study on erosion–corrosion degradation of pipework located on an offshore oil and gas facility, Wear, 271 (2011) 1295-1301.
[30] X. Hu, K. Alzawai, A. Gnanavelu, A. Neville, C. Wang, A. Crossland, J. Martin, Assessing the effect of corrosion inhibitor on erosion–corrosion of API-5L-X65 in multi-phase jet impingement conditions, Wear, 271 (2011) 1432-1437.
[31] X.M. Hu, The corrosion and erosion-corrosion behavior of high alloy stainless steels, The University of Leeds, Leeds, UK, 2002.
[32] A. Gnanavelu, N. Kapur, A. Neville, J.F. Flores, An integrated methodology for predicting material wear rates due to erosion, Wear, 267 (2009) 1935-1944.
[33] X.W. Chen, G.Y. Qiao, X.L. Han, X. Wang, F.R. Xiao, B. Liao, Effects of Mo, Cr and Nb on microstructure and mechanical properties of heat affected zone for Nb-bearing X80 pipeline steels, Materials & Design, 53 (2014) 888-901.
[34] S. Morito, X. Huang, T. Furuhara, T. Maki, N. Hansen, The morphology and crystallography of lath martensite in alloy steels, Acta Materialia, 54 (2006) 5323-5331.
[35] Z.J. Luo, J.C. Shen, H. Su, Y.H. Ding, C.F. Yang, X. Zhu, Effect of Substructure on Toughness of Lath Martensite/Bainite Mixed Structure in Low-Carbon Steels, J Iron Steel Res Int, 17 (2010) 40-48.
[36] B.T. Lu, J.L. Luo, Correlation between surface-hardness degradation and erosion resistance of carbon steel—Effects of slurry chemistry, Tribology International, 83 (2015) 146-155.
[37] A. Madhan Kumar, N. Rajendran, Influence of zirconia nanoparticles on the surface and electrochemical behaviour of polypyrrole nanocomposite coated 316L SS in simulated body fluid, Surface and Coatings Technology, 213 (2012) 155-166.
[38] M. Multigner, S. Ferreira-Barragans, E. Frutos, M. Jaafar, J. Ibanez, P. Marin, M.T. Perez-Prado, G. Gonzalez-Doncel, A. Asenjo, J.L. Gonzalez-Carrasco, Superficial severe plastic deformation of 316 LVM stainless steel through grit blasting: Effects on its microstructure and subsurface mechanical properties, Surf Coat Tech, 205 (2010) 1830-1837.
[39] T. Balusamy, S. Kumar, T.S.N. Sankara Narayanan, Effect of surface nanocrystallization on the corrosion behaviour of AISI 409 stainless steel, Corrosion Science, 52 (2010) 3826-3834.
[40] V. Barranco, E. Onofre, M.L. Escudero, M.C. Garcia-Alonso, Characterization of roughness and pitting corrosion of surfaces modified by blasting and thermal oxidation, Surf Coat Tech, 204 (2010) 3783-3793.
[41] A. Gnanavelu, A geometry independent integrated method to predict erosion wear rates in a slurry environment, The University of Leed, leeds,UK, 2010.

[42] R. Kaul, P. Ganesh, P. Tiwari, R.V. Nandedkar, A.K. Nath, Characterization of dry sliding wear resistance of laser surface hardened En 8 steel, Journal of Materials Processing Technology, 167 (2005) 83-90.
[43] J.S. Selvan, K. Subramanian, A.K. Nath, Effect of laser surface hardening on En18 (AISI 5135) steel, Journal of Materials Processing Technology, 91 (1999) 29-36.

Figure captions

Figure 1: Jet impingement system for erosion-corrosion test including in-situ electrochemical monitoring instrument.

Figure 2: SEM images of sand particles (a) before the test and (b) after the test

Figure 3: Top view of the test sample after testing viewed under the naked eye indicating three distinctive regions of wear and also the CFD predictions of particle motion [32].

Figure 4: Surface profile measurement results of specimens after erosion-corrosion.

Figure 5: Local erosion-corrosion rate around indentation.

Figure 6: Local sand impact data at the surface of specimen in Forties Brine at 20 m/s.

Figure 7: Erosion-corrosion rates as a function of impact angle.

Figure 8: Erosion-corrosion morphology in region with impact angle high to medium range. (a) $\alpha=90°$ (as-supplied X65); (b) $\alpha=90°$ (laser-treated X65); (c) $60°<\alpha<70°$ (as-supplied X65); (d) $60°<\alpha<70°$ (laser-treated X65); (e) $42°<\alpha<45°$ (as-supplied X65); (f) $42°<\alpha<45°$ (laser-treated X65).

Figure 9: Erosion-corrosion morphology in the zone with impact angle medium to low range. (a) $35°<\alpha<40°$ (as-supplied X65); (b) $35°<\alpha<40°$ (laser-treated X65); (c) $30°<\alpha<35°$ (as-supplied X65); (d) $30°<\alpha<35°$ (laser-treated X65).

Figure 10: Erosion-corrosion morphology in the zone with very low impact angle. (a) as-supplied X65; (b) laser-treated X65.

Figure 11: Subsurface morphology of erosion-corrosion indentation.

Figure 112: Microstructure of as-supplied X65 steel. (a) optical microscopic observation; (b) TEM observation.

Figure 13: EDX analysis of precipitates (phase A in Figure 9(b)).

Figure 14: Microstructure of laser-treated X65 steel. (a) full view; (b) melted zone; (c) coarse grains near fusion line; (d) fine grains; (e) partially refined grains.

Figure 15: Martensite contents in laser-treated X65 steel.

Figure 16: TEM micrographs of laser melted X65 steel. (a) microstructure; (b) selected area electron diffraction of B in (a).

Figure 17: Hardness distribution in cross section of laser-treated X65 steel specimen. (a) location of test

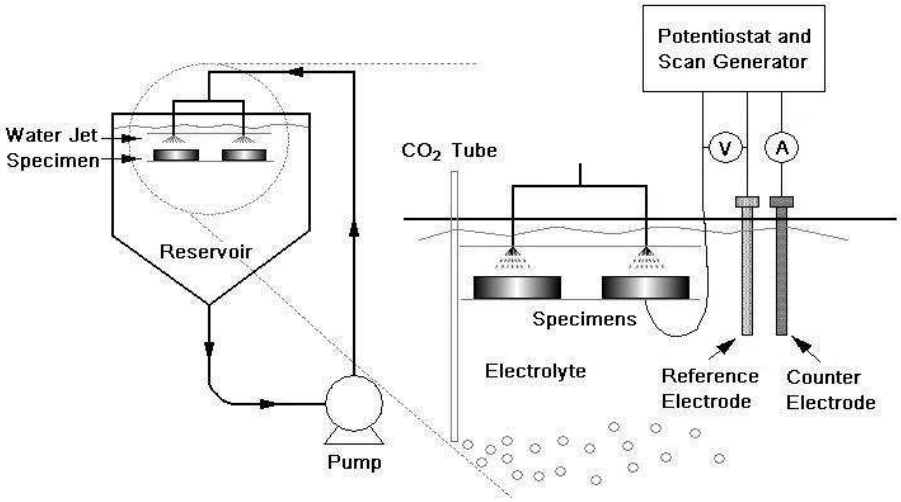

Figure 1 Jet impingement system for erosion-corrosion test including in-situ electrochemical monitoring instrument.

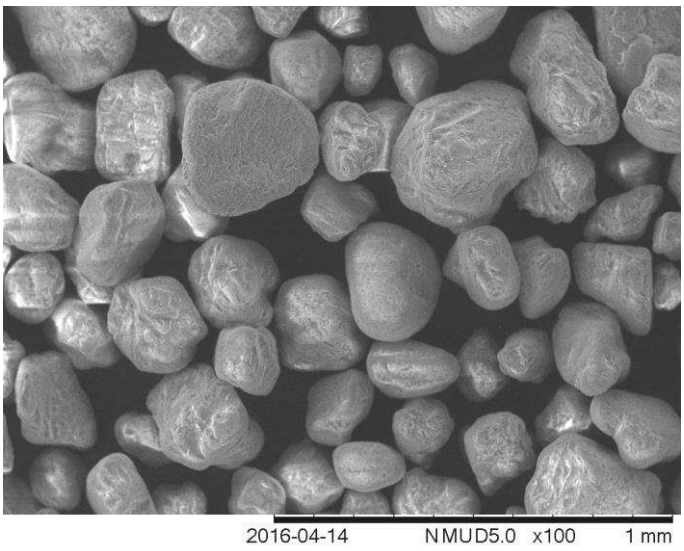

(a)

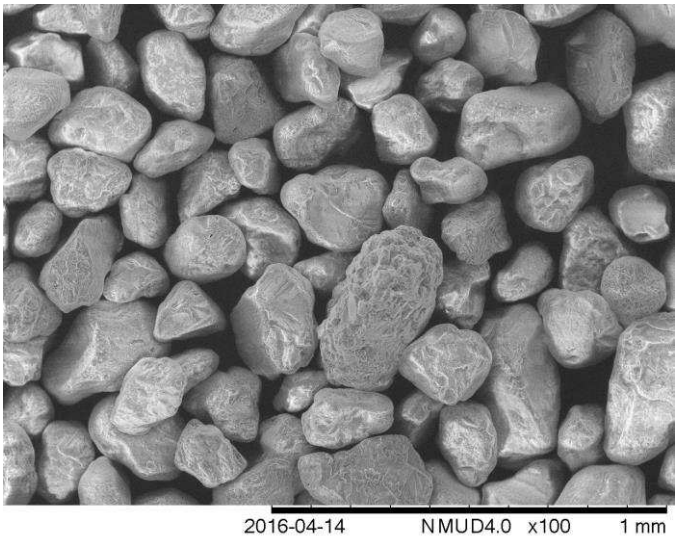

(b)

Figure 2 SEM images of sand particles comparison (a) before and (b) after the test

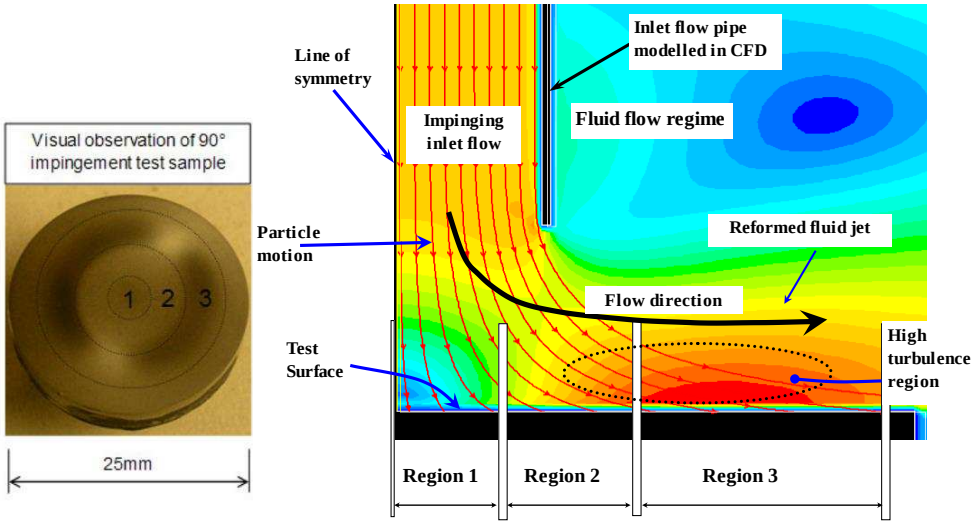

Figure 3 Top view of the test sample after testing viewed under the naked eye indicating three distinctive regions of wear and also the CFD predictions of particle motion [32].

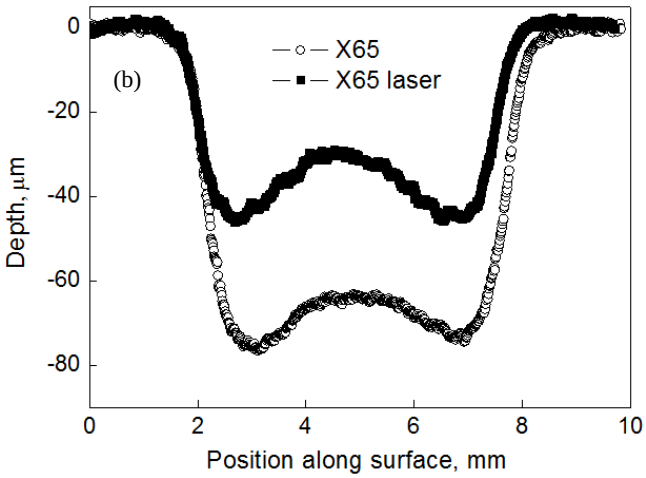

Figure 4 Surface profile measurement results of specimens after erosion-corrosion.

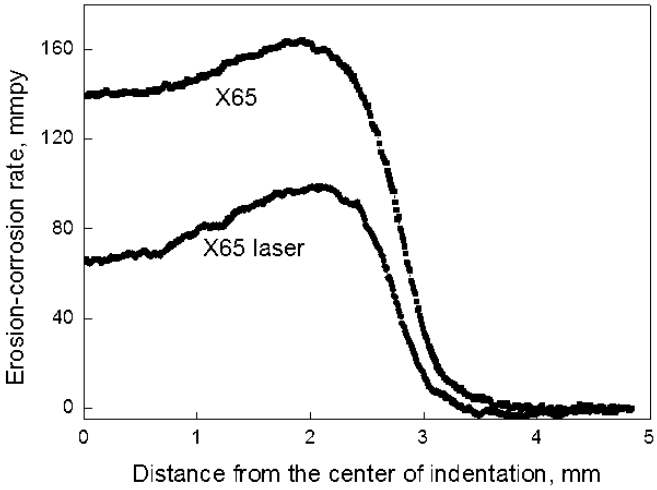

Figure 5 Local erosion-corrosion rates around indentation.

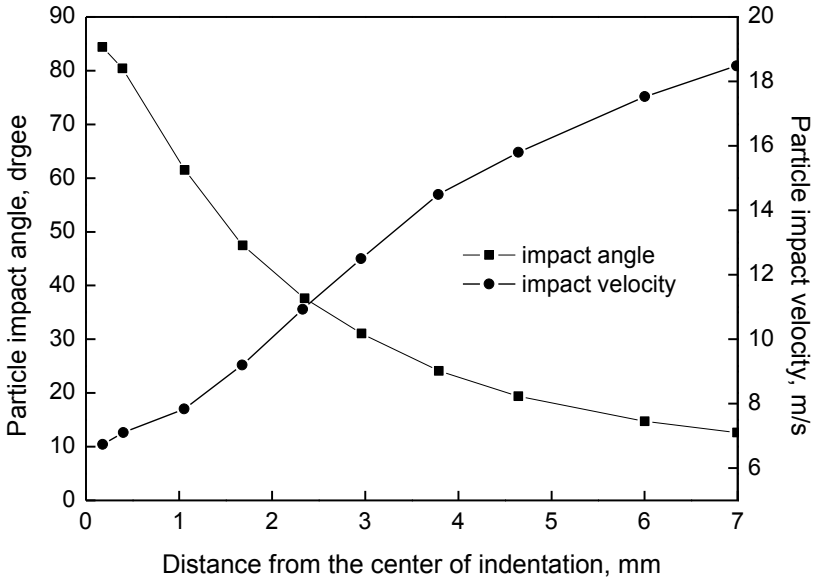

Figure 6 Local sand impact data at the surface of specimen in Forties Brine at 20 m/s.

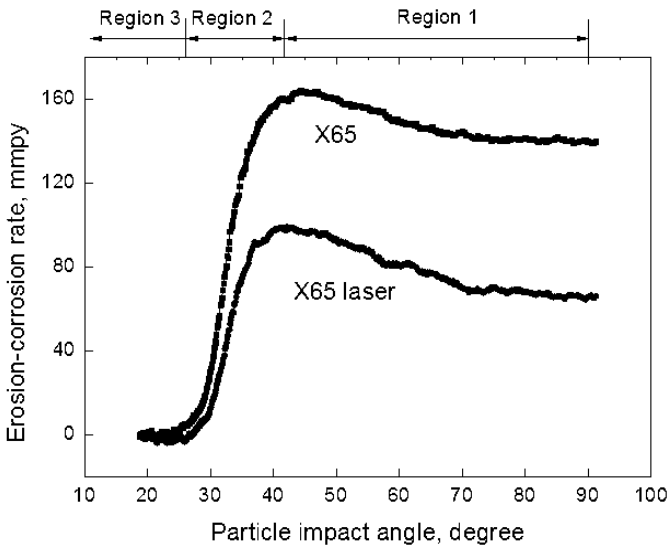

Figure 7 Erosion-corrosion rates as a function of impact angle.

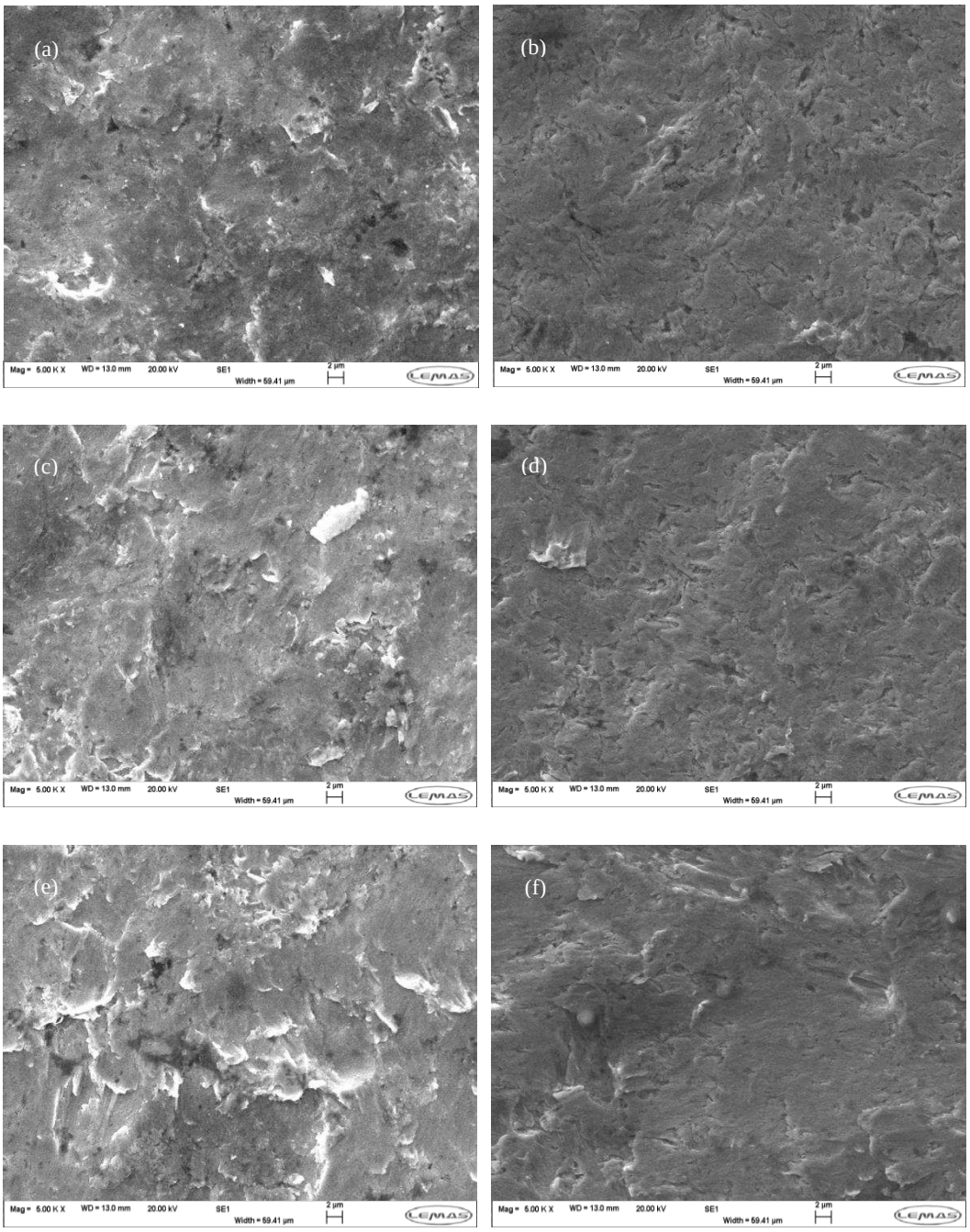

Figure 8 Erosion-corrosion morphology in region with impact angle high to medium range. (a) $\alpha=90°$ (as-supplied X65); (b) $\alpha=90°$ (laser-treated X65); (c) $60°<\alpha<70°$ (as-supplied X65); (d) $60°<\alpha<70°$ (laser-treated X65); (e) $42°<\alpha<45°$ (as-supplied X65); (f) $42°<\alpha<45°$ (laser-treated X65).

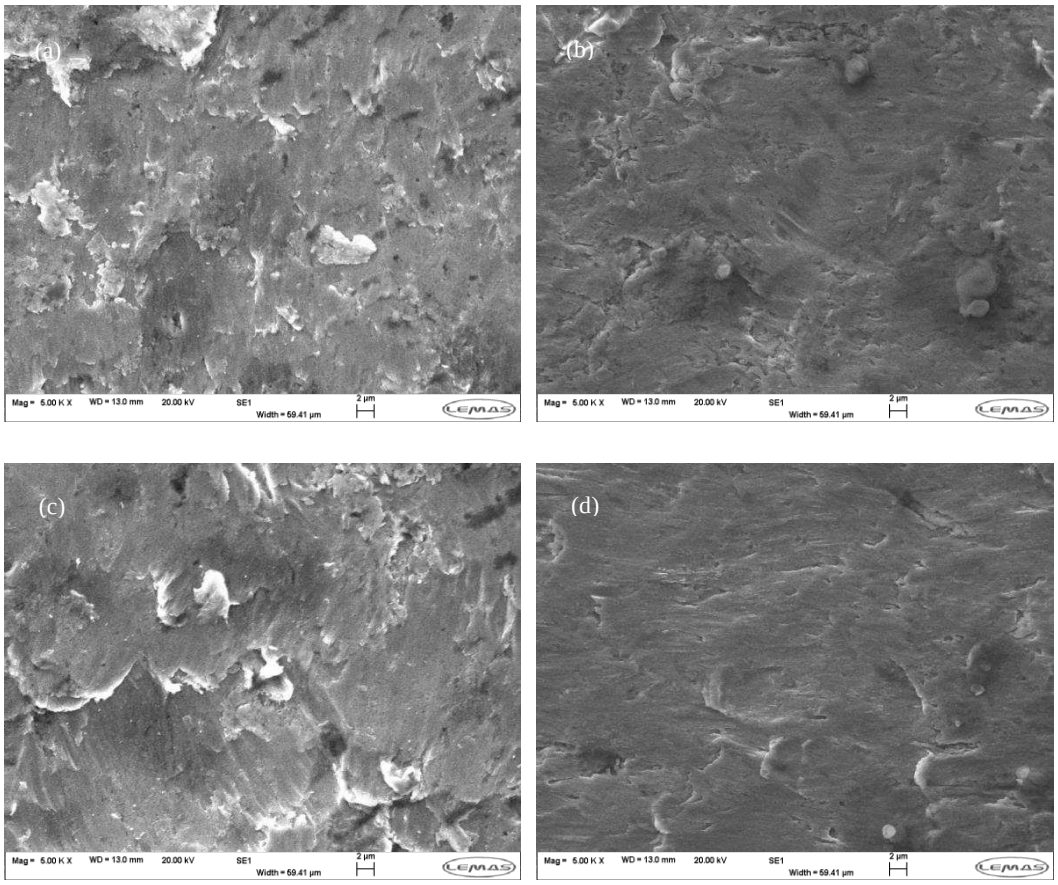

Figure 9 Erosion-corrosion morphology in the zone with impact angle medium to low range. (a) 35°<α<40° (as-supplied X65); (b) 35°<α<40° (laser-treated X65); (c) 30°<α<35° (as-supplied X65); (d) 30°<α<35° (laser-treated X65).

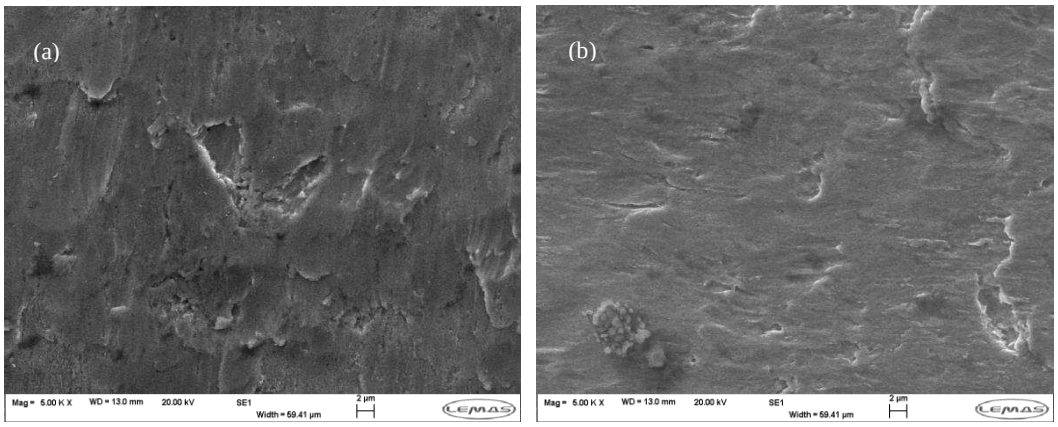

Figure 10 Erosion-corrosion morphology in the zone with very low impact angle. (a) as-supplied X65; (b) laser-treated X65.

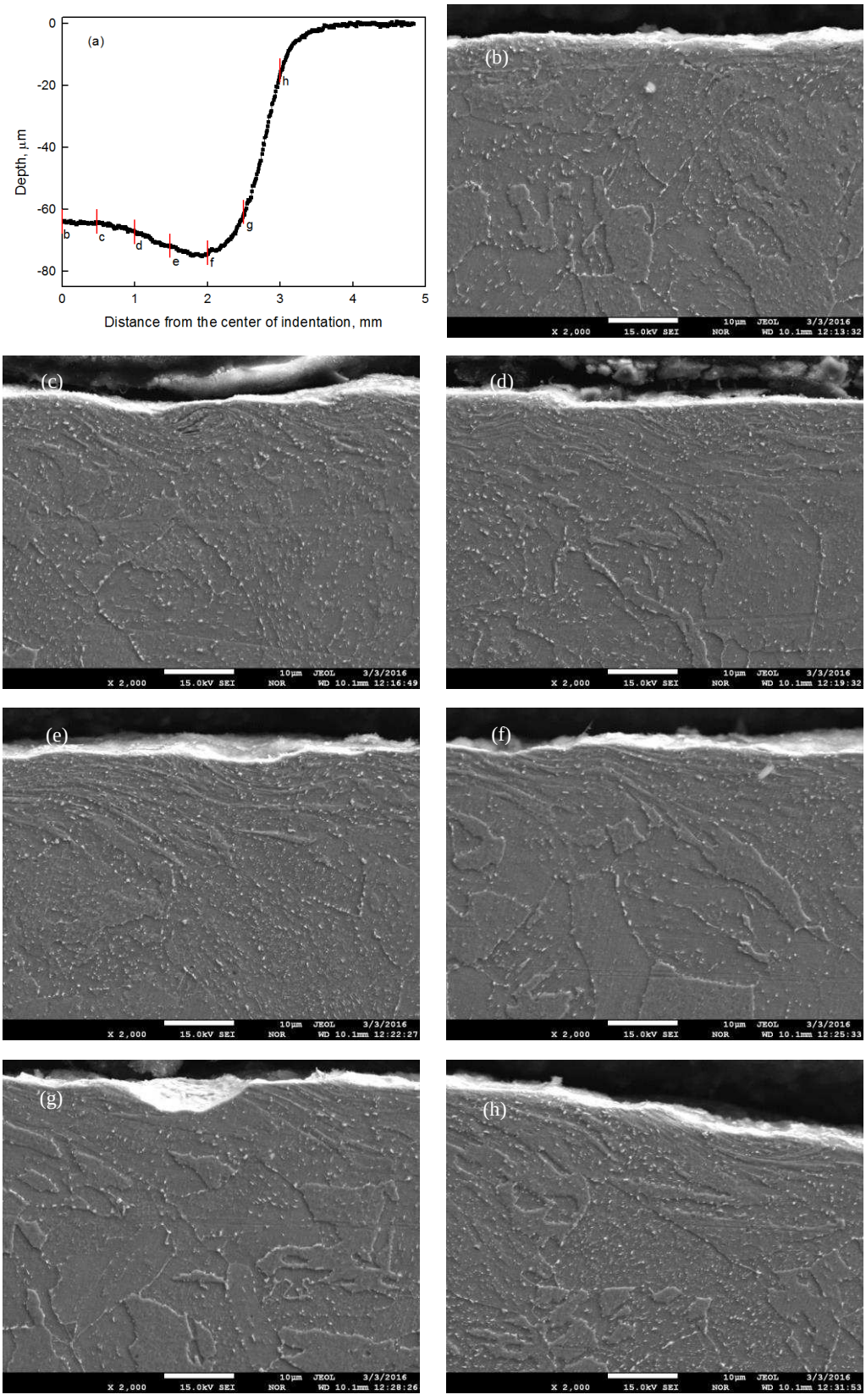

Fig. 11 Subsurface morphology of erosion-corrosion indentation

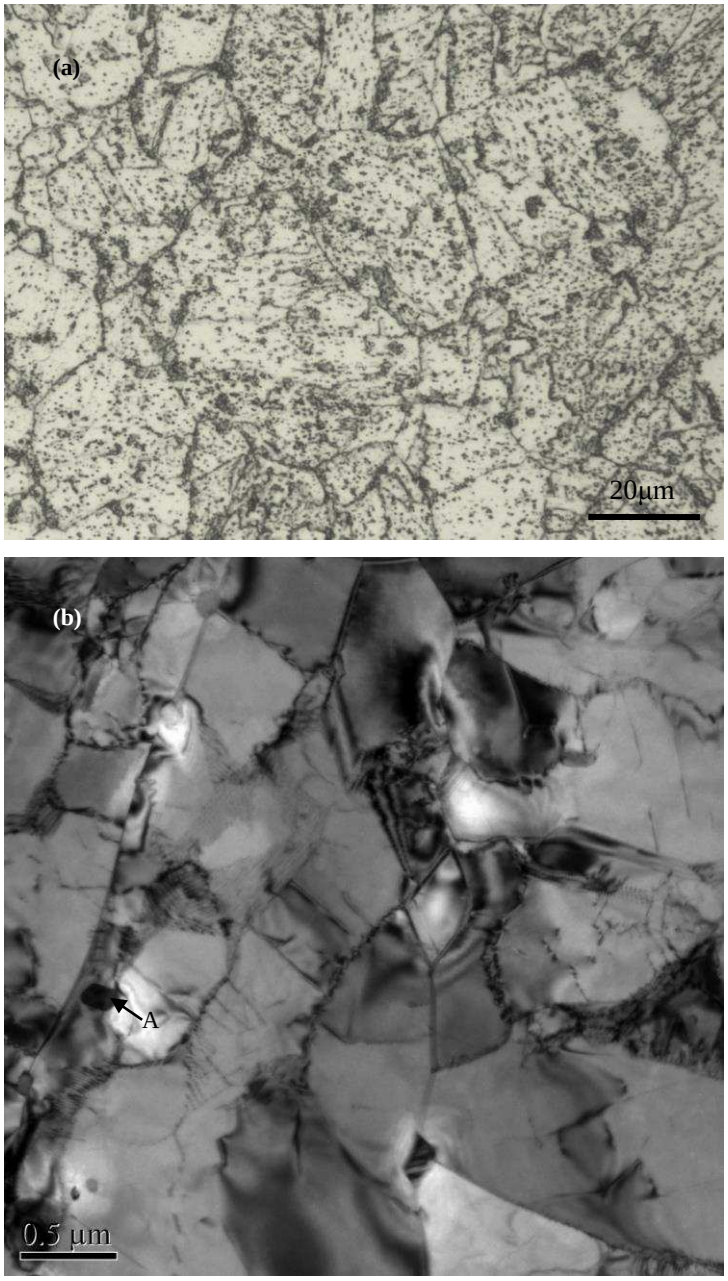

Figure 12 Microstructure of as-supplied X65 steel. (a) optical microscopic observation; (b) TEM observation.

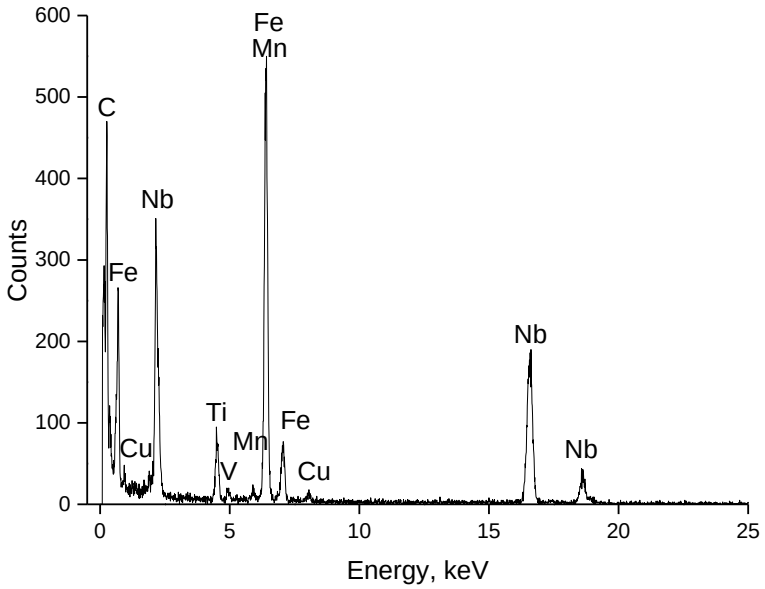

Figure 13 EDX analysis of precipitates (phase A in Figure 9(b)).

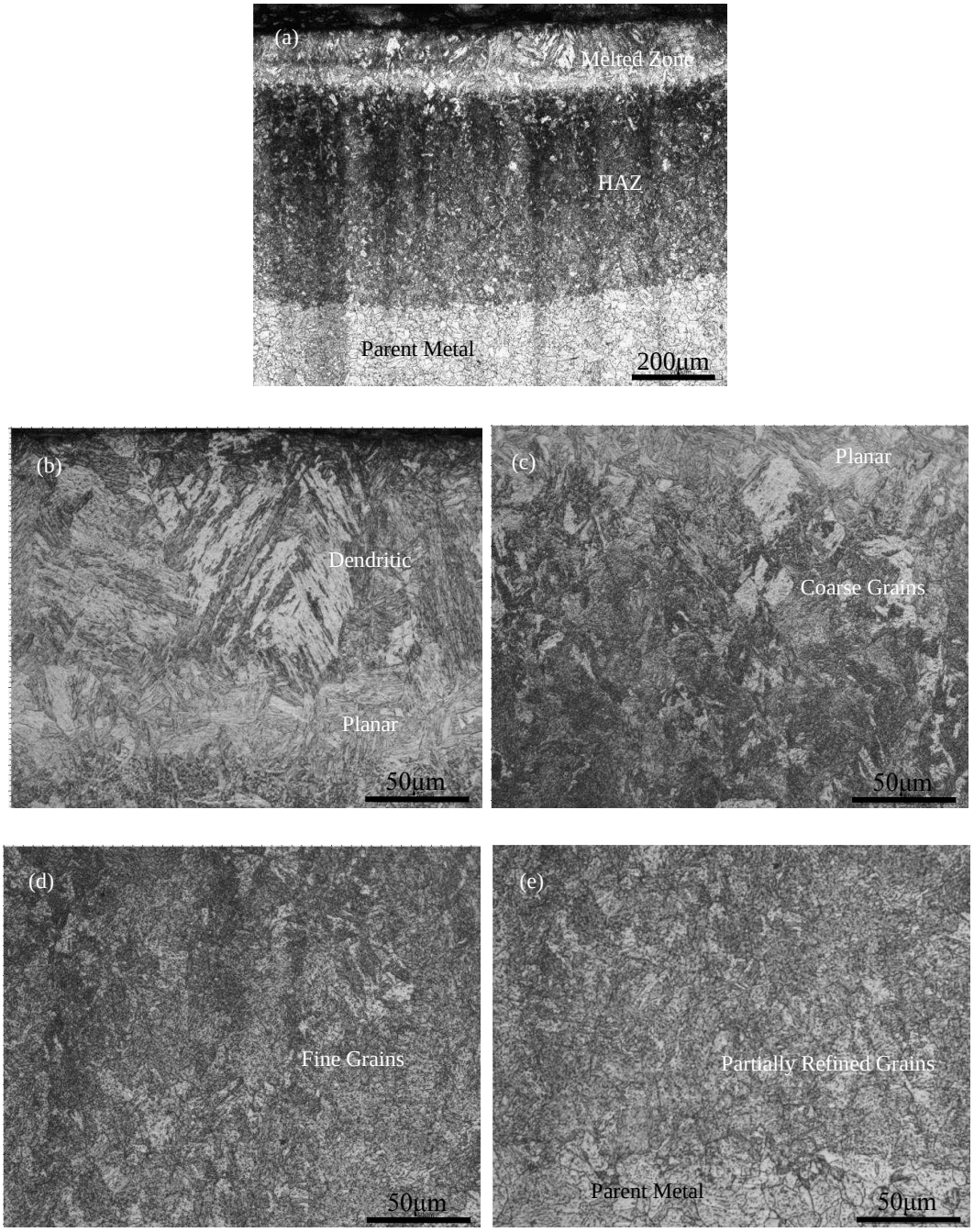

Figure 14 Microstructure of laser-treated X65 steel. (a) full view; (b) melted zone; (c) coarse grains near fusion line; (d) fine grains; (e) partially refined grains.

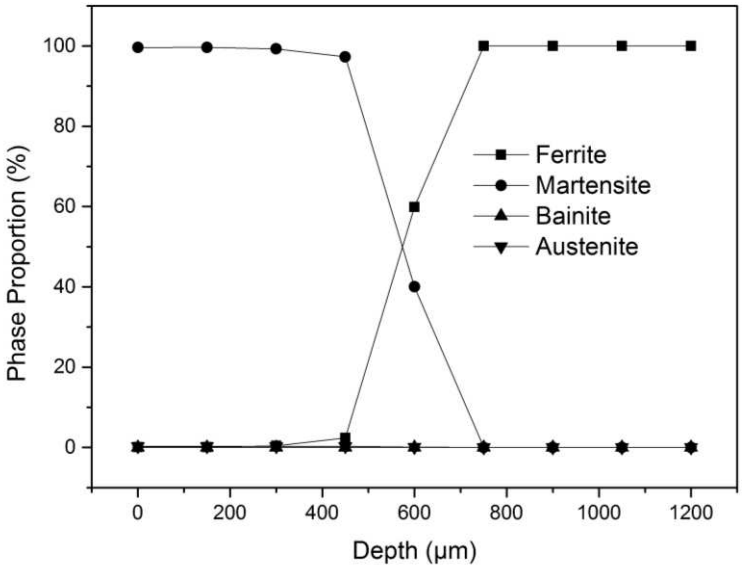

Figure 15 Martensite contents in laser-treated X65 steel.

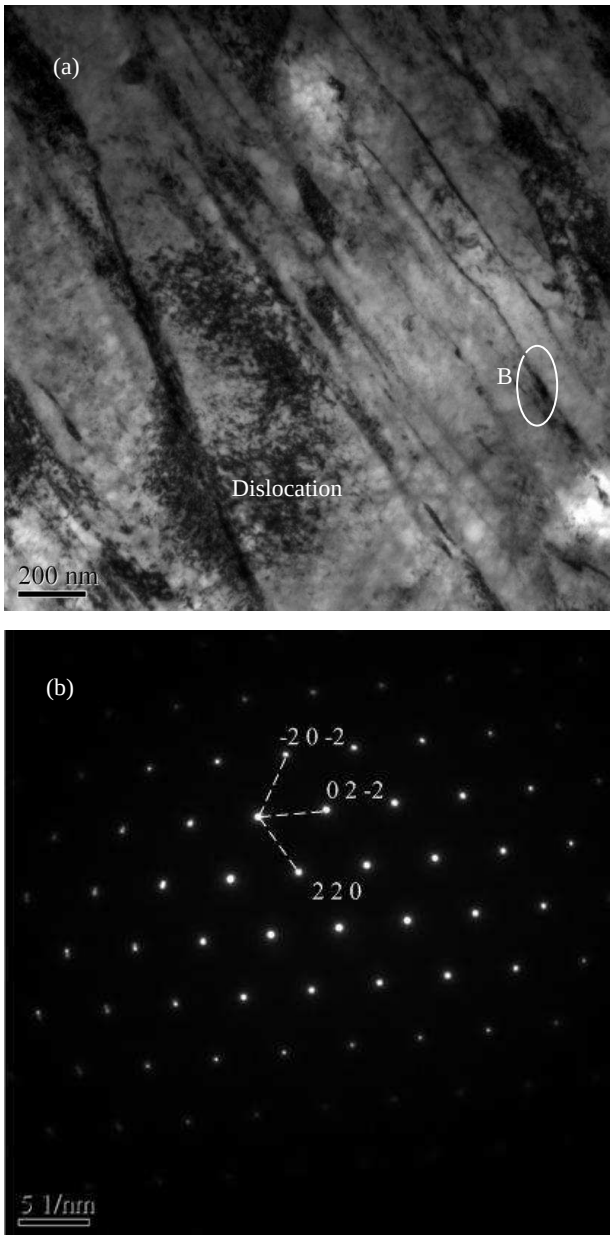

Figure 16 TEM micrographs of laser melted X65 steel. (a) microstructure; (b) selected area electron diffraction of B in (a).

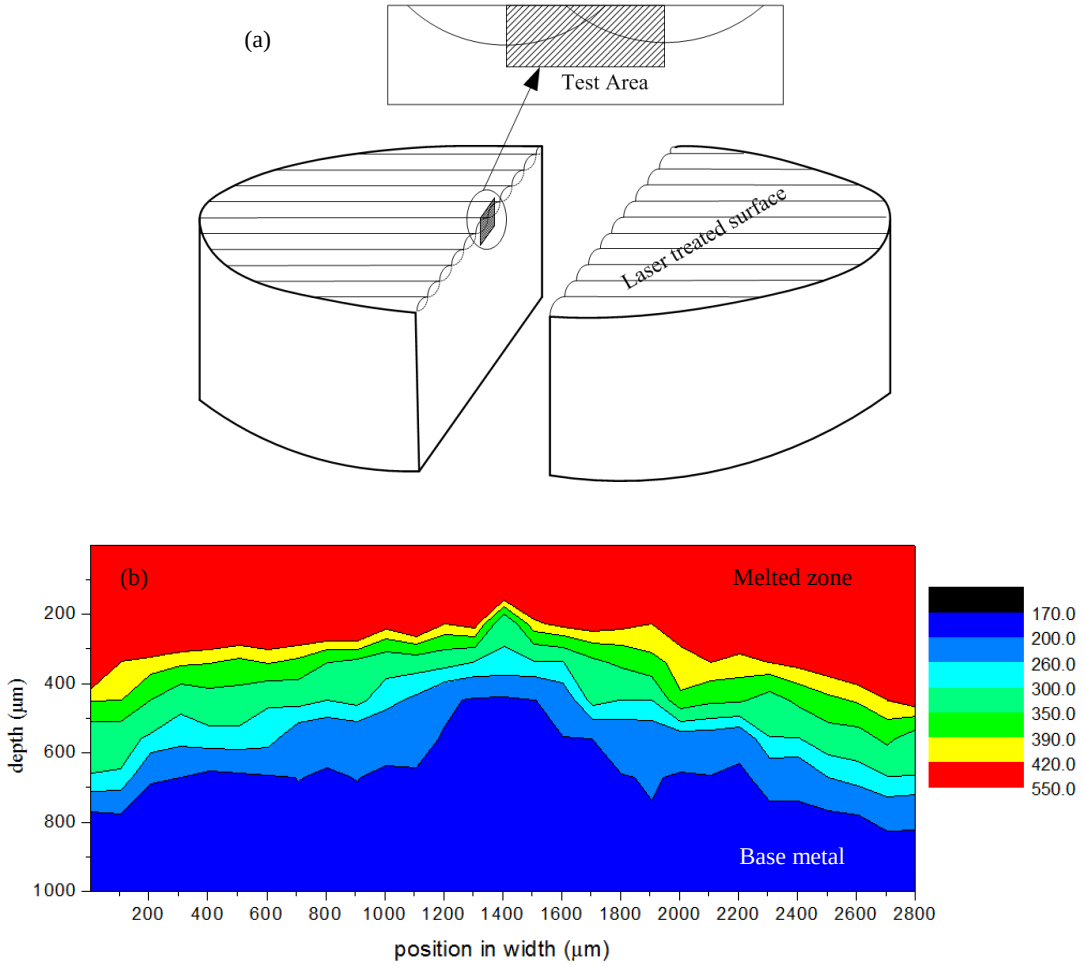

Figure 17 Hardness distribution in cross section of laser-treated X65 steel specimen. (a) location of test area; (b) hardness distribution.

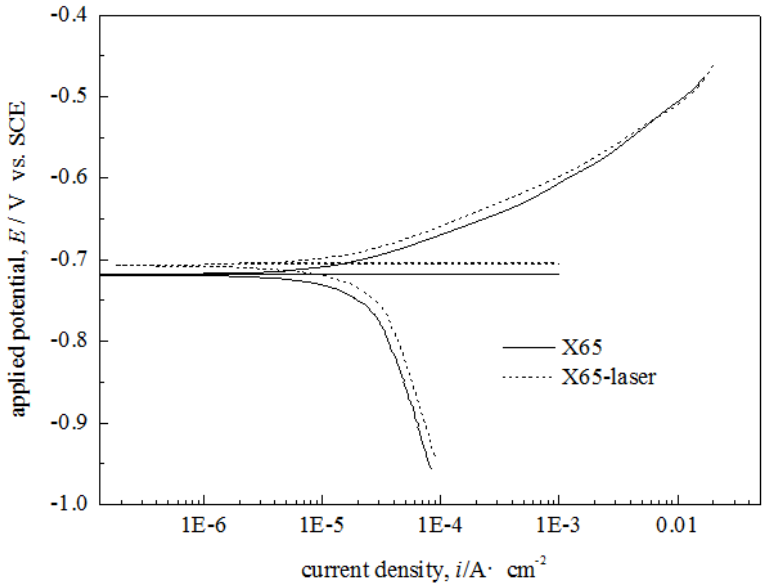

Figure 18 Tafel polarization curves of X65 steel under different state in static Forties Brine.

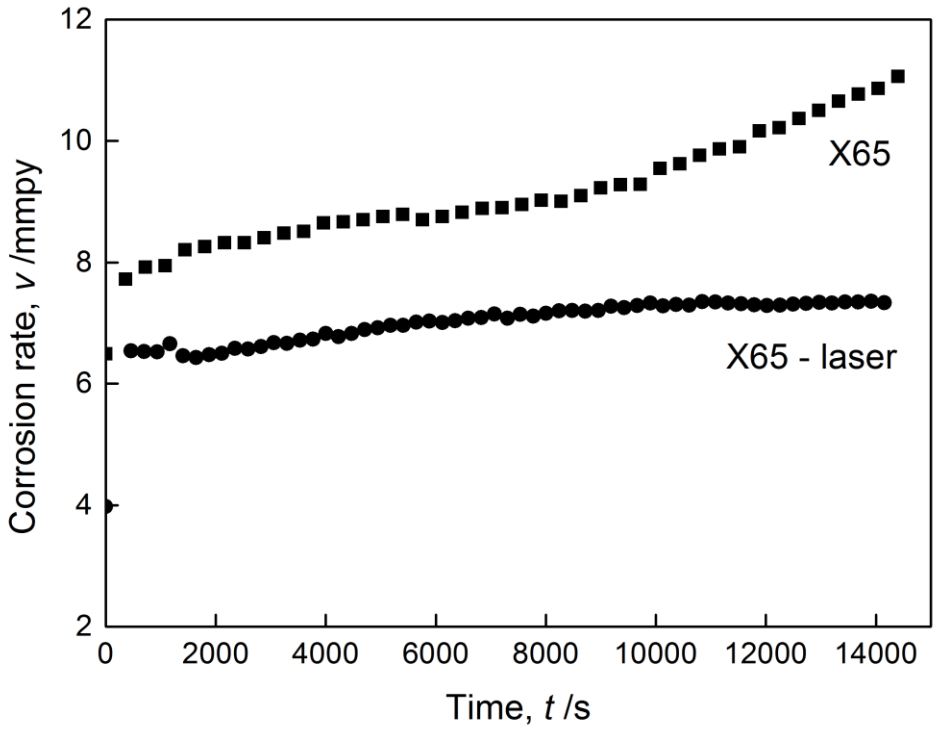

Figure 19 Corrosion rate deduced from the LPR results as a function of time under erosion-corrosion conditions.

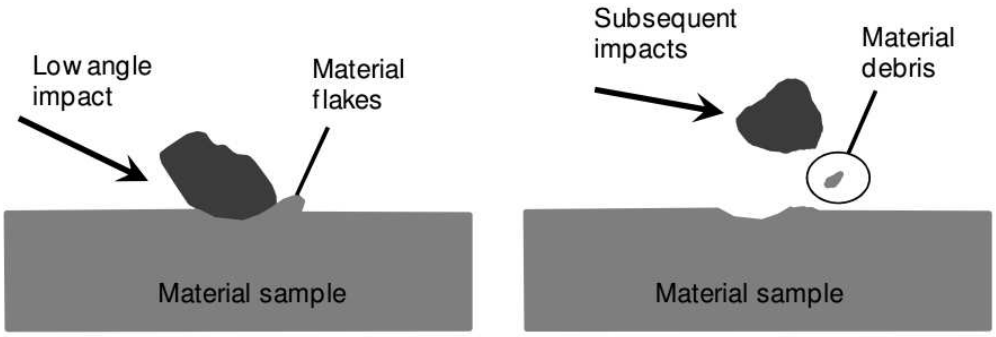

Figure 20 Material removal mechanism due to impact of solid particles at medium to low impact angles in ductile material.